Z. Phys. A 345, 231–242 (1993)

ZEITSCHRIFT
FÜR PHYSIK A

The effects of electron screening and resonances in (p, α) reactions on ^{10}B and ^{11}B at thermal energies

C. Angulo, S. Engstler, G. Raimann, C. Rolfs, W.H. Schulte, E. Somorjai*

Institut für Physik mit Ionenstrahlen, Ruhr-Universität Bochum, Postfach 102148, W-4630 Bochum 1, Germany

Received: 20 October 1992

Abstract. The fusion reactions $^{10}B(p, \alpha)\,^{7}Be$ and $^{11}B(p, \alpha)\,^{8}Be$ have been studied over the c.m. energy range $E = 17$ to 134 keV using intense proton beams and thick solid targets. In the case of $^{11}B(p, \alpha)\,^{8}Be$ the low-energy data in terms of the astrophysical $S(E)$ factor show an exponential enhancement (up to a factor of 1.9) due to the effects of electron screening, where the deduced screening potential is larger than expected. In the case of $^{10}B(p, \alpha)\,^{7}Be$ the low-energy data exhibit an enhancement by more than a factor of 200, which cannot be explained by the effects of electron screening. The enhancement arises here from the high-energy tail of an expected s-wave resonance at $E_R = 10$ keV. The results offer an improved prospect for this reaction as advanced fuel in future fusion reactors than previously envisioned.

PACS: 25.40.

1. Introduction

The cross section $\sigma(E)$ of fusion reactions drops steeply at energies far below the Coulomb barrier. To extrapolate the data to the energies of hydrostatic burning phases in various astrophysical scenarios (essentially to zero energy), it is advantageous to transform the cross section into the astrophysical $S(E)$ factor defined by the relation [1]

$$\sigma(E) = S(E)\,E^{-1}\exp(-2\pi\eta), \tag{1}$$

where $2\pi\eta = 31.29\,Z_1 Z_2 (\mu/E)^{1/2}$ is the Sommerfeld parameter (Z_1 and Z_2 = charge numbers of the interacting nuclides, μ = reduced mass in amu, E = c.m. energy in keV). In the case of reactions involving light nuclides, the $S(E)$ factor often varies slowly with energy.

In (1) it is assumed that the Coulomb potential of the target nucleus is that resulting from bare nuclei, and thus the potential would extend to infinity. However, for nuclear reactions studied in the laboratory, the target nuclei are usually in the form of neutral atoms or molecules. The atomic (or molecular) electron cloud surrounding the target nucleus acts [2] as a screening potential: an incoming charged projectile experiences no repulsive Coulomb force until it penetrates the electron cloud; thus, the projectile sees a reduced Coulomb barrier. This in turn leads to a higher cross section, $\sigma_s(E)$, than would be the case for bare nuclei, $\sigma_b(E)$, with an enhancement factor [2]

$$f(E) = \sigma_s(E)/\sigma_b(E) \simeq \exp(\pi\eta U_e/E), \tag{2}$$

where U_e is the constant electron screening potential energy (e.g. $U_e \simeq Z_1 Z_2 e^2/R_a$, with R_a an atomic radius). Note that $f(E)$ increases exponentially with decreasing incident energy. For energy ratios $E/U_e \geqq 1000$, shielding effects are negligible, and laboratory experiments can be regarded as essentially measuring $\sigma_b(E)$. However, for $E/U_e \leqq 100$, shielding effects cannot be neglected and become important for understanding low-energy data. Relatively small enhancements from electron screening at energy ratios $E/U_e \simeq 100$ can cause significant errors [3] in the extrapolation of cross sections to lower energies, if the curve of the cross section is forced to follow the trend of the enhanced cross sections, without correction for the screening. Notice that for astrophysical and other applications (stellar and terrestrial fusion plasmas) the value of $\sigma_b(E)$ must be known because the screening in these applications is quite different from that in laboratory nuclear reaction studies, and $\sigma_b(E)$ must be explicitly included for each situation [2]. Recent low-energy studies of the reactions $^{3}He(d,p)\,^{4}He$ [4] and $^{6}Li(p,\alpha)\,^{3}He$, $^{6}Li(d,\alpha)\,^{4}He$, and $^{7}Li(p,\alpha)\,^{4}He$ [5] have shown clearly such screening effects, as well as their dependence on the aggregate state of the target. It was also

Supported in part by the Deutsche Forschungsgemeinschaft (Ro429/18-2 and Ro429/21-3) and the Comision Interministerial de Ciencia y Tecnologia (AEN90-0932)

* *Permanent address:* Institute of Nuclear Research, Hungarian Academy of Sciences, Debrecen, Hungary

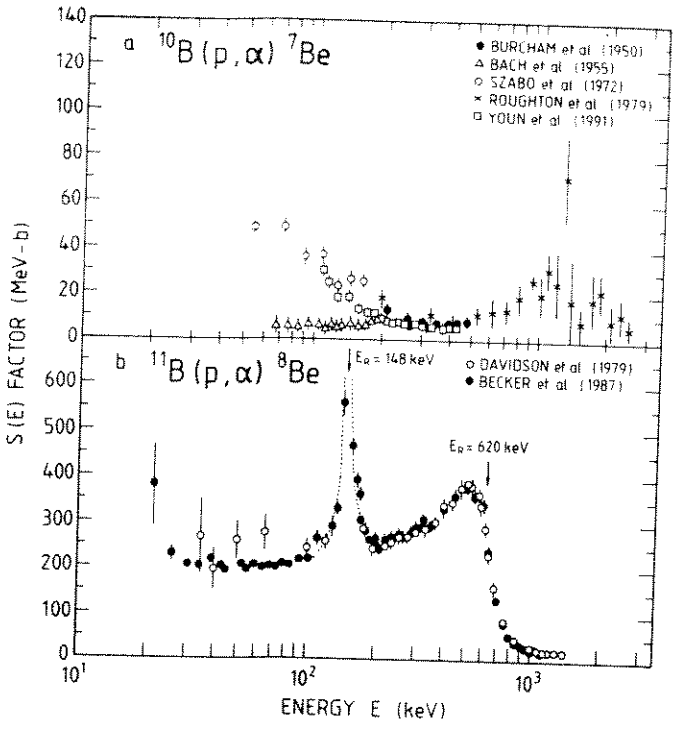

Fig. 1a, b. Published data for the fusion reactions $^{10}B(p,\alpha)^{7}Be$ [9–13] and $^{11}B(p,\alpha)^{8}Be$ [14–15] are shown in form of the astrophysical $S(E)$ factor. The $^{11}B(p,\alpha)^{8}Be$ data near the top of the $E_R = 148$ keV resonance have been omitted, and the absolute cross sections reported by Davidson et al. [14] have been increased by a factor 3/2 (see [15]). Further, the thick target yields reported by Roughton et al. [12] have been converted to thin target yields by subtracting yields from adjacent energies; the resulting yields together with stopping power data [19] provided then the absolute cross sections (or $S(E)$ factors) for $^{10}B(p,\alpha)^{7}Be$ as shown in **a** (see also Sect. 4.8)

found [5] that the screening potential was independent from the isotopic character of the target nuclides, as expected from simple models. However, the deduced values for the screening potential U_e were significantly larger than expected from models. The difference between the observed and expected U_e values (i.e. larger screening effects than expected) is presently not understood. Clearly, a thorough understanding of screening effects requires additional efforts in theory [6–8] as well as in experiment, where improved low-energy data for other fusion reactions are needed.

The fusion reactions $^{10}B(p,\alpha)^{7}Be$ and $^{11}B(p,\alpha)^{8}Be$, with respective Q values of 1.146 and 8.591 MeV, are both of interest for the understanding of their nucleosynthetic origin [1] as well as for advanced fuels in future fusion reactors [16]. The published total cross sections for the $^{10}B(p,\alpha)^{7}Be$ [9–13] and $^{11}B(p,\alpha)^{8}Be$ [14, 15] reactions are shown in Fig. 1 in form of the $S(E)$ factor (here: $2\pi\eta(^{10}B+p) = 149.7\,E^{-1/2}$ and $2\pi\eta(^{11}B+p) = 150.3\,E^{-1/2}$). The available data for $^{11}B(p,\alpha)^{8}Be$ are in excellent agreement – within experimental uncertainties – in the energy dependence as well as in the absolute scale. At the lowest energies there are some indications of the effects of electron screening, but the errors are too large to draw any meaningful conclusions. In contrast, the data for $^{10}B(p,\alpha)^{7}Be$ allow no clear picture for the behavior of $S(E)$ at low energies: firstly, the energy dependence and the absolute scale of the various data sets differ in part significantly at overlapping energy regions, and, secondly, the experiments have not been carried out to sufficiently low energies (or/and with sufficient precision) in order to observe clearly the effects of electron screening. For these reasons, a renewed measurement of both reactions was carried out in the present work, using an intense proton beam and thick boron solid targets. All details of the work not presented here can be found in [17, 18].

2. Formalism

For an incident energy E_0, a target thickness Δ, and a stopping power $\varepsilon(E)$ (all in c.m. system), the observed number of counts in a detector placed at θ_{lab}, $N(E,\theta_{lab})$, is related to the cross section $\sigma(E)$ via the equation [1]

$$N(E_0,\theta_{lab}) = (4\pi)^{-1}(1+\delta)\,N_p\,\Omega_{lab}\,\kappa \times \int_a^b K_\Omega(E,\theta)\,W(E,\theta)\,\sigma(E)\,\varepsilon(E)^{-1}\,dE, \quad (3)$$

where $\delta = 0$ (or $\neq 0$) in the case of non-identical (or identical) ejectiles (here: $\delta = 0$ for $^{10}B(p,\alpha)^{7}Be$, and $\delta = 1$ for $^{11}B(p,\alpha)^{8}Be(2\alpha)$, see [15]). The quantity N_p is the number of incident projectiles, and Ω_{lab} and κ are the solid angle and efficiency of the detector, resepctively (here: $\kappa = 1$ for Si detectors). The transformation of solid angle between the c.m. and lab system is described by $K_\Omega(E,\theta)$ and the angular distribution by $W(E,\theta)$, where E and θ are c.m. coordinates. The available data show [13–15, 28] that $W(E,\theta)$ is isotropic (or nearly so) at the relevant low energies for both fusion reactions, thus $W(E,\theta) = 1$ is assumed here. The integration limits in (3) are $a = E_{min} = E_0 - \Delta$ and $b = E_{max} = E_0$. If $K_\Omega(E,\theta)$ is approximately constant over Δ, (3) simplifies in the present work to

$$N(E_0,\theta_{lab}) = (4\pi)^{-1}(1+\delta)\,N_p\,\Omega_{lab}\,K_\Omega(E_0,\theta)\,Y(E_0), \quad (4)$$

where the reaction yield per incident projectile, $Y(E_0)$, is given by

$$Y(E_0) = \int_a^b \sigma(E)\,\varepsilon(E)^{-1}\,dE. \quad (5)$$

Further, if $\sigma(E)$ and $\varepsilon(E)$ are also approximately constant over Δ, one arrives at the thin target yield [1]

$$Y(E_0) = \sigma(E_0)\,\varepsilon(E_0)^{-1}\,\Delta = \sigma(E_0)\,N_a, \quad (6)$$

where N_a is the number of active target nuclides per cm^2. If $\sigma(E)$ is not constant over Δ, but $\varepsilon(E)$ and $S(E)$ are constant over Δ, one finds (using (1))

$$Y(E_0) = S(E)\,\varepsilon(E)^{-1} \int_{E_{min}}^{E_{max}} \exp(-2\pi\eta)\,E^{-1}\,dE$$

$$= 2\,S(E)\,\varepsilon(E)^{-1} \int_{E}^{E_{max}} \exp(-2\pi\eta)\,(E^*)^{-1}\,dE^*, \quad (7)$$

where the effective energy E, defined by this equation, corresponds [1] to that energy within the target, at which one-half of the reaction yield is obtained. This effective energy is then associated with the deduced value of the $S(E)$ factor, or equivalently of $\sigma(E)$. Finally, for an infinitely thick target one has $E_{min} = 0$ and the extraction of $S(E)$, or $\sigma(E)$, from the observed count rates requires a different approach (Sect. 4.8).

In the target consists of several elements, with N_a active target nuclides and N_i inactive target nuclides of species i (all in units of atoms/cm^2), the target thickness Δ (in units of eV) is described by an effective target thickness Δ_{eff} given by

$$\Delta_{eff} = N_a\,\varepsilon_a(E) + \Sigma_i N_i\,\varepsilon_i(E) = N_a\,\varepsilon_{eff}(E), \quad (8)$$

where $\varepsilon_a(E)$ and $\varepsilon_i(E)$ are the stopping powers [19] (in units of eV atom^{-1} cm^2) of the active and inactive nuclides at energy E, respectively, and the effective stopping power $\varepsilon_{eff}(E)$ is described by

$$\varepsilon_{eff}(E) = \varepsilon_a(E) + \Sigma_i (N_i/N_a)\,\varepsilon_i(E). \quad (9)$$

Further, if the beam is not monoenergetic in the interval from E_{min} to E_{max}, as assumed in the above equations, but is described by an energy distribution, one has to fold [1] the above integral with this distribution.

In addition to a sufficient number of counts, say $N(E_0, \theta_{lab}) = 1000$ (3.2% statistical error), a precise determination of $S(E)$ requires a good knowledge of the quantities N_p, Ω_{lab}, E_{max}, E_{min}, $W(E,\theta)$, N_a, N_i, Δ_{eff} and $\varepsilon_{eff}(E)$, where applicable. The determination of these experimental parameters is described in the following sections.

3. Experimental equipment and setup

The experimental equipment and setup are similar to those described recently [5]. Thus, only the essential features as well as differences are described briefly.

3.1. Accelerators

The 100 and 400 kV accelerators at the Dynamitron Tandem Laboratorium of the Ruhr-Universität Bochum provided H_1^+, H_2^+, and H_3^+ ion beams in the proton energy range[1] $E_p = 17$ to 150 keV. At the lowest energies, the proton beam current (for H_3^+) was 1.5 mA, while at the highest energies the current was limited to a few μA by dead time effects in the detectors (kept below 2%). The uncertainty in absolute energy, ΔE_{lab}, and the energy spread, ξ_{lab}, were ±26 and 20 eV for the 100 kV accelerator and ±1.0 and 1.0 keV for the 400 kV accelerator, respectively. The error in absolute energy for the 100 kV accelerator at the lowest energy led to an uncertainty in cross section of 3.3%.

For chemical and isotopic analyses of the boron targets (Sect. 4), the 350 kV accelerator in Münster and the 4MV Dynamitron tandem accelerator in Bochum were also used, providing beams of protons ($E_p = 0.14$ to 1.0 MeV), deuterons ($E_d = 0.92$ MeV), ^{4}He ions ($E_\alpha = 7.6$ MeV), and ^{19}F ions ($E_F = 6.4$ to 8.0 MeV).

3.2. Setups

For the measurement of excitation functions for both fusion reactions, a setup in close geometry was used. The setup in the $^{11}B(p,\alpha)^8Be$ studies was identical to that reported recently [5, 17]. However, for the $^{10}B(p,\alpha)^7Be$ measurements a new cylindrical target chamber (17 cm diameter, 30 cm length) was designed, which had additional features such as the possibility of in situ analyses of the target stoichiometry via backscattering spectroscopy (BS) and nuclear reaction analyses (NRA) (Sect. 4).

In this new setup, the hydrogen beam passed first through two watercooled Ta apertures A_1 and A_2, which defined the beam direction (A_1: 19 or 13 mm diameter at the 100 or 400 kV accelerators, A_2: 13 mm diameter with an antiscattering aperture of 14 mm diameter closeby, 80 cm distance between both apertures). The beam was focussed on the target into a spot of about 15 mm diameter. For the in situ target analyses, the diameter of the apertures A_1 and A_2 was reduced to 13 and 2 mm, respectively, with a beam spot on target of about 2 mm diameter. A liquid-nitrogen (LN_2) cooled in-line Cu tube (65 cm length, 2.7 cm inner diameter) extended from near the aperture A_2 to within about 4 cm of the target. With this tube and two turbo-pumps (with 150 and 360 l/s pumping speeds) no carbon-buildup on the target was observed (pressure in the target chamber: $p_t = 5 \times 10^{-7}$ mbar). The apertures A_1 and A_2, the Cu tube, and the target were electrically insulated; the beam currents measured at these components were used to optimize the beam profile on target.

The boron target (5 cm diameter, with direct water cooling applied to the Ta backing) was oriented with its normal antiparallel to the beam direction. For the $^{10}B(p,\alpha)^7Be$ studies the boron target was enriched[2] to 93% in ^{10}B (with remaining 7% ^{11}B), and for the $^{11}B(p,\alpha)^8Be$ studies the boron target was of natural isotopic composition (19.9% ^{10}B, 80.1% ^{11}B). Due to high sputtering rates at low energies (Sect. 4.5), the boron targets were fabricated with a thickness in the range of 60 to 107 μg/cm^2, i.e. thicker than the range of low-energy protons in the target (e.g. a proton beam of 30 keV is stopped in a 30 μg/cm^2 boron target). The fabrication of the boron targets was carried out in the following way. Firstly, the 0.3 mm thick Ta backing was heated in

[1] In what follows all energetic quantities such as projectile energy, resonance energy, resonance width, target thickness, etc. are in the lab system, except where indicated otherwise

[2] Supplier: Union Carbide Corporation, Oak Ridge, Tennessee, USA

vacuum to about 2000 °C for several minutes, to clean its surface. Secondly, the original boron material (a powder) was pressed into pellets of a few mm diameter and evaporated onto the Ta backing using an electron gun (25 cm distance between the pellet and the Ta backing). During the evaporation in vacuum (pressure $\leqq 1\times10^{-6}$ mbar) the Ta backing was heated to about 100 °C, to enhance the sticking of the boron film on the backing. The evaporated boron film thickness was monitored with a quartz oscillator gauge. Thirdly, after fabrication the targets were stored in a container filled with Ar gas.

The emitted α-particles from both fusion reactions were observed with 4 surface barrier (Si) detectors positioned at $\theta_{lab}=130°$ around the beam axis. In this arrangement the summed number of counts of the 4 detectors was nearly independent from the actual location and diameter of the beam spot on target. The detectors were electrically insulated from the target chamber and covered with Ni foils to stop the intense flux of elastically scattered particles. The target together with the chamber and the detector holders (including the Ni foils) formed the Faraday cup for beam integration. A negative voltage of 300 V was applied to the Cu tube for suppression of secondary electrons. It was estimated that the beam current was measured with a precision of about $\pm 3\%$.

In the $^{10}B(p,\alpha)^{7}Be$ measurements at low energies, the target chamber was surrounded by a 5 cm thick lead shield, and a plastic scintillator of 1.2 m^2 area and 5 cm thickness was placed above the target chamber; both components were used to identify and reduce the contributions of cosmic rays and room background, leading [18] to one order of magnitude improvement in the signal-to-noise ratio for the relevant α-detection. A similar setup was used in the $^{11}B(p,\alpha)^{8}Be$ studies (for details, see [5]).

For the measurement of in situ stoichiometry of fresh and bombarded boron targets (Sect. 4), the target-end-station was sealed with 2 valves, transported from the 100 kV accelerator to the 400 kV and 4 MV accelerators (and viceversa), and installed at a beam-line jointly used by both accelerators. During the 1 h transport time, the LN_2 shroud maintained a vacuum in the target chamber of better than $p_t=1\times10^{-4}$ mbar. The targets were then bombarded with various projectiles at energies, at which the Ni foils in front of the 4 Si detectors could not stop the elastically scattered projectiles. For this reason the new target chamber allowed to retract these 4 detectors via a sledge (mechanical feedthrough) far away from the target such that the beam spot on target was shadowed for them by the in-line Cu pipe. For these in situ measurements, two additional Si detectors were placed in the new target chamber, one at $\theta_{lab}=165°$ (for BS) and the other at $\theta_{lab}=135°$ (for NRA). These detectors were also electrically insulated from the target chamber. The NRA-detector was covered with a Ni foil of 7 μm thickness, to stop 1 MeV deuterons.

3.3. Detectors

As discussed above the α-particle yields from the $^{10}B(p,\alpha)^{7}Be$ reaction were measured at $\theta_{lab}=130°$ using 4 Si detectors, which were partially depleted with the following characteristics: active area $=600\ mm^2$, effective thickness $=300$ μm, Al contact layer $=50$ nm, Si dead layer $=100$ nm, energy resolution $=22$ keV at $E_\alpha=5.5$ MeV. The detectors were placed at a mean distance of $d\simeq40$ mm from the target, with an opening angle of $\Delta\theta_{lab}=\pm19°$. The total solid angle of the 4 detectors was determined [18] using a calibrated α-source leading to $\Omega_{lab}=1.26\pm0.01$ sr, in good agreement with geometrical estimates. The detectors were covered with Ni foils

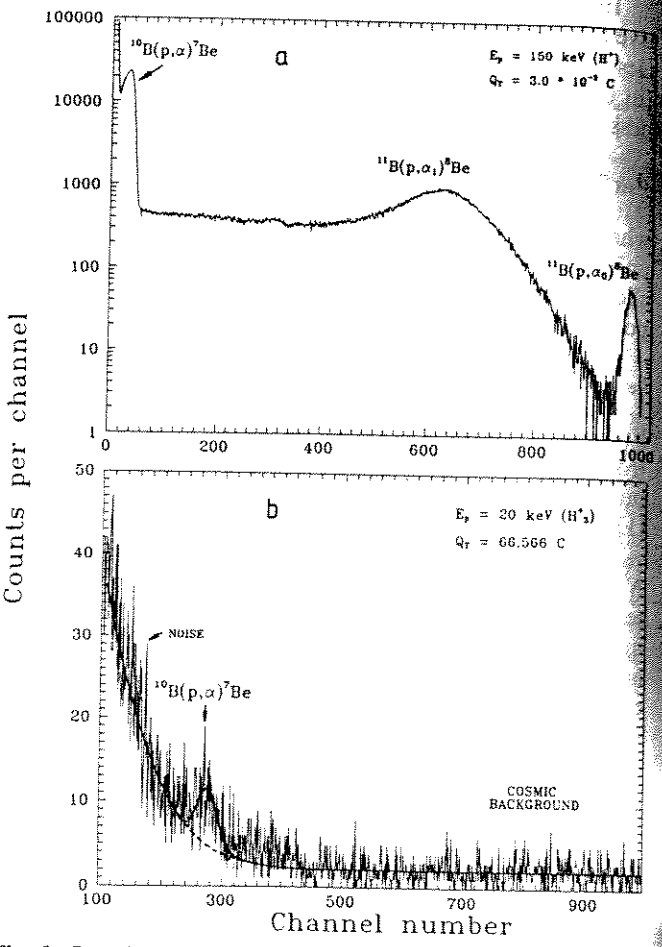

Fig. 2. Sample spectra obtained with one of the 4 Si detectors (placed at $\theta_{lab}=130°$ and covered with a Ni foil) by proton bombardment of an enriched ^{10}B target at the **a** highest energy ($E_p=150$ keV, H_1^+ beam, 0.50 μm thick Ni foil) and **b** lowest energy ($E_p=20$ keV, H_3^+ beam, 0.25 μm thick Ni foil) of the present $^{10}B(p,\alpha)^{7}Be$ investigations. The accumulated charge Q_T on target is also given. Note that the α-peak from $^{10}B(p,\alpha)^{7}Be$ is always close to the "noise" region of the spectrum, where its location and width is consistent [18] with effects of energy loss, kinematic broadening, and energy straggling in the target, Ni foil, Al contact layer, and Si dead layer. The noise arises probably from pile-up effects of secondary electrons in the detector. The curves through the data points in **b** are the results of a description [18] of *(i)* the noise by an exponential function, *(ii)* the cosmic background by a constant yield, and *(iii)* the relevant α-peak by Gaussian functions. Note the logarithmic scale in **a**

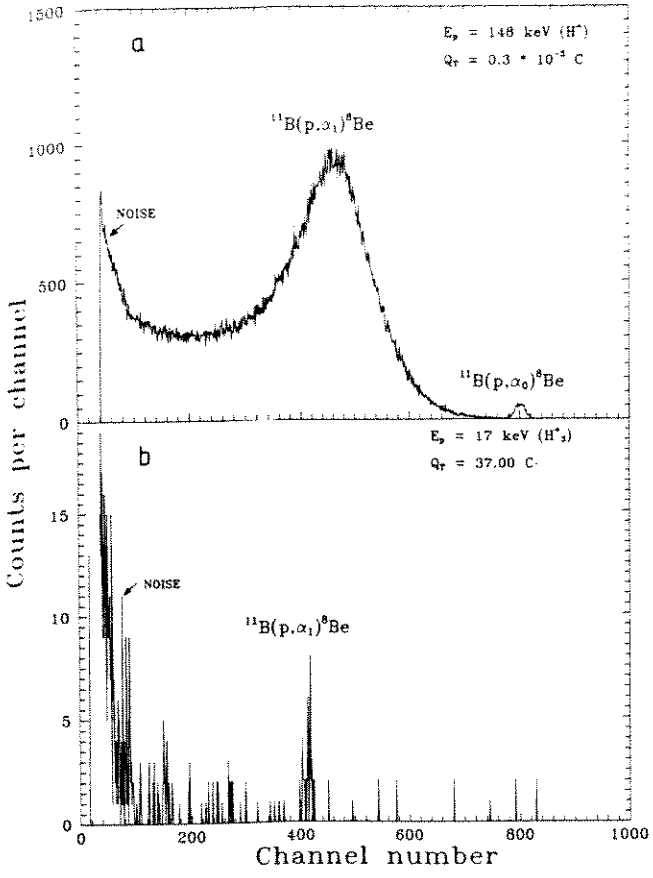

Fig. 3. Sample spectra obtained with one of the 4 Si detectors (placed at $\theta_{lab} = 130°$ and covered with a 2.0 μm thick Ni foil) by proton bombardment of a boron target of natural isotopic composition at the **a** highest energy ($E_p = 148$ keV, H_1^+ beam) and **b** lowest energy ($E_p = 17$ keV, H_3^+ beam) of the present $^{11}B(p,\alpha)^8Be$ investigations. The accumulated charge Q_T on the target is also given. Note that the α-group from $^{10}B(p,\alpha)^7Be$ is here not visible due to absorption in the Ni foil (compare Fig. 2). The narrow peak near channel 400 arises from the contaminant reaction $d(d,p)t$ due to a natural deuterium-component in the H_3^+ molecular beam

of 0.25 and 0.50 μm thickness at $E_p = 17$ to 30 and 30 to 150 keV, respectively. In the $^{11}B(p,\alpha)^8Be$ studies [17], the detectors had an active area of 450 mm², with $\Delta\theta_{lab} = \pm 16°$ and $\Omega_{lab} = 0.92 \pm 0.01$ sr, and were covered with 2 μm thick Ni foils. Sample spectra obtained at the highest and lowest energies for both fusion reactions are shown in Figs. 2 and 3.

For the backscattering spectroscopy (BS) the partially depleted Si detector (placed at $\theta_{lab} = 165°$) had an active area of 50 mm², an effective thickness of 100 μm, and an energy resolution of 12 keV at $E_\alpha = 5.5$ MeV. The detector was placed at a distance $d = 17$ cm from the target and was collimated by an aperture of 5 mm diameter in front of the detector. With the calibrated source the solid angle was found to be $\Delta\Omega_{lab} = 0.58 \pm 0.03$ msr, consistent with geometry. During the studies of the $^{10}B(p,\alpha)^7Be$ reaction at the 100 and 400 kV accelerators, this BS detector could not see the target since it was shadowed by the housings of the 4 Si detectors.

The Si detector used for NRA was placed at $\theta_{lab} = 135°$ ($d = 58$ mm, 125 mm² active area, 15 keV energy resolution) and collimated by a 10 mm diameter aperture in front of the detector. With the calibrated α-source a value of $\Omega_{lab} = 23 \pm 1$ msr was found, again consistent with geometry.

In the NRA measurements via the reactions $^{16}O(p,\gamma)^{17}F$ (Sect. 4.3) and $^1H(^{19}F,\alpha\gamma)^{16}O$ (Sect. 4.6), the γ-rays were observed with a 145 cm³ Ge detector placed at $\theta_\gamma = 0°$ in close geometry ($d = 1.5$ cm). The absolute photopeak efficiency $\Omega_{lab}\kappa = \kappa(E_\gamma)$ was determined [18] at $E_\gamma = 0.2$ to 6.8 MeV via calibrated γ-ray sources as well as the isotropic γ-rays from the $E_R = 278$ keV resonance in $^{14}N(p,\gamma)^{15}O$. The results are well described by the analytic expression $\kappa(E_\gamma) = 14.5 \times 10^{-3} \exp(-0.384 E_\gamma)$, with E_γ in MeV and $\Delta\kappa/\kappa \leqq \pm 10\%$. Finally, the boron target thickness was measured using the $E_R = 162$ keV resonance in $^{11}B(p,\gamma)^{12}C$ (Sect. 4.2), where a 10.2 cm diameter x 10.2 cm NaI(Tl) crystal was placed at $\theta_\gamma = 0°$ in close geometry ($d = 1.5$ cm).

4. Experimental procedures, data analyses and results

4.1. Isotopic composition of the ^{10}B enriched targets

The isotopic composition of the ^{10}B enriched targets was measured [18] via the relative α-yields of the $^{11}B(p,\alpha)^8Be$ reaction at $E_p = 60$ keV using an enriched ^{10}B target and a target of natural boron composition with respective thicknesses of 67 and 48 keV (e.g., Figs. 2a and 3a). The resulting abundances of $92.8 \pm 0.2\%$ ^{10}B and $7.2 \pm 0.2\%$ ^{11}B are in excellent agreement with the quotation of the supplier (93% ^{10}B and 7% ^{11}B). These results are also consistent with other measurements (see below).

4.2. Thickness of the boron targets

Preliminary experiments at $E_p \leqq 50$ keV using "thin" boron targets (of order of several μg/cm²) showed that the target deteriorated fast: the reaction yield at a fixed energy decreased more than a factor of 2 within a few Coulombs of accumulated charge on the target. This decrease is caused by the sputtering process having high probabilities at these low energies [19]. For this reason, "infinitely thick" boron targets at these energies (greater than 60 μg/cm²) were fabricated (Sect. 3.2), minimizing thus the sputtering effects on the observed α-yields (see however Sect. 4.5). Three enriched boron targets were used for the $^{10}B(p,\alpha)^7Be$ studies, and 2 boron targets of natural isotopic composition were used for the $^{11}B(p,\alpha)^8Be$ studies (Table 1).

The thickness of all "fresh" targets was determined using the $E_R = 162$ keV resonance ($\Gamma_R = 5.8$ keV) in $^{11}B(p,\gamma)^{12}C$. The resulting thick-target yield curve for target #1 (Table 1) is shown in Fig. 4; when the non-resonant yield (due to the $E_R = 675$ keV resonance) is taken into account (dashed line in Fig. 4), the yield curve shows a nearly homogeneous boron distribution starting at the target surface and extending into the target with a thickness of $\Delta_{eff} = 67 \pm 2$ keV (derived from the 50% points at both sides of the yield curve). The results for all 5 boron targets are summarized in Table 1.

Table 1. Summary of target characteristics

Nr.	Thickness[a] ($\mu g/cm^2$)	Δ_{eff}[b] (keV)	N_O[c] (10^{17})	N_B[f] (10^{18})	N_B[g] (10^{18})	N_B[h] (10^{18})	N_C[i] (10^{16})	N_O/N_B[k] (%)
^{10}B enriched targets[l]								
1	100	67 ± 2	4.0 ± 0.5[d]	4.9 ± 0.5	4.4 ± 0.5	4.7 ± 0.3	3.8 ± 0.4	8.5
2	86	54 ± 2	3.3 ± 0.4[d]	4.0 ± 0.4	3.9 ± 0.5	4.0 ± 0.3	4.5 ± 0.5	8.3
3	107	69 ± 2	5.4 ± 0.6[d]	5.0 ± 0.7	5.4 ± 0.5	5.2 ± 0.4	2.5 ± 0.3	10.4
Boron targets of natural isotopic composition[m]								
4	80	48 ± 2	4.1 ± 0.4[e]	3.4 ± 0.3	[n]	3.4 ± 0.3	[n]	12.1
5	60	38 ± 2	2.8 ± 0.3[e]	2.8 ± 0.3	[n]	2.8 ± 0.3	[n]	10.0

[a] From quartz oscillator gauge measurements (Sect. 3.2)
[b] From $E_R = 162$ keV resonance in $^{11}B(p,\gamma)^{12}C$ (Sect. 4.2)
[c] Number of ^{16}O nuclides (in units of 10^{17} atoms/cm^2)
[d] From elastic scattering at $E_\alpha = 7.60$ MeV (Sect. 4.3)
[e] From $^{16}O(p,\gamma)^{17}F$ at $E_p = 1.00$ MeV (Sect. 4.3)
[f] Number of boron nuclides (in units of 10^{18} atoms/cm^2) calculated from columns 3 and 4
[g] Number of boron nuclides (in units of 10^{18} atoms/cm^2) from (d,p) and (d,α) reactions at $E_d = 0.92$ MeV (Sect. 4.4)
[h] Adopted value of boron nuclides (in units of 10^{18} atoms/cm^2)
[i] Number of ^{12}C nuclides (in units of 10^{16} atoms/cm^2) from (d,p) reaction at $E_d = 0.92$ MeV (Sect. 4.4)
[k] From columns 4 and 7
[l] $^{10}B = 93\%$, $^{11}B = 7\%$ (Sect. 4.1)
[m] $^{10}B = 19.9\%$, $^{11}B = 80.1\%$
[n] Not determined

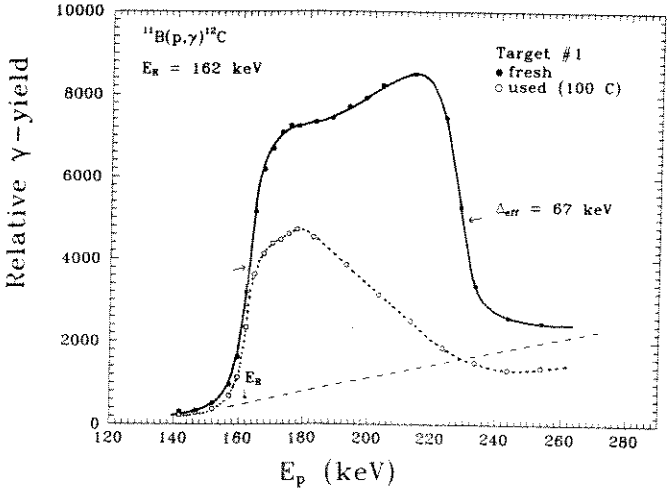

Fig. 4. Thick-target yield curve of a "fresh" ^{10}B enriched target (#1) using the $E_R = 162$ keV resonance in $^{11}B(p,\gamma)^{12}C$ (filled-in data points), leading to a target thickness of $\Delta_{eff} = 67$ keV. The open data points represent the respective yield curve of this target, after a bombardment by low-energy protons with 100 C of accumulated charge ("used" target). The curves through the data points are to guide the eye only

4.3. *Oxygen content in the boron targets*

Due to the infinitely thick and heavy Ta backing, light elements in the boron film (target) such as oxygen cannot be detected via the usual Rutherford backscattering spectroscopy (RBS) using ^{4}He ions of $E_\alpha = 1$ to 2 MeV. However, the $^{16}O(\alpha,\alpha)^{16}O$ elastic scattering cross section shows [20] at backward angles a broad resonance structure at $E_\alpha = 7.3$ to 7.7 MeV with a nearly constant cross section, which is enhanced by a factor of 130 compared to the Rutherford scattering law (e.g., $(d\sigma/d\Omega)_{lab} = 690$ mb/sr at $\theta_{lab} = 165°$). A spectrum obtained with the BS-detector ($\theta_{lab} = 165°$) at $E_\alpha = 7.60$ MeV for a fresh boron target (#1) is shown in Fig. 5a: one sees the infinitely thick Ta backing as a nearly flat plateau with a sharp high-energy edge, where this edge is shifted to lower energies by the boron film thickness on the target surface (see also Sect. 4.6). Superimposed on the plateau are peaks corresponding to ^{16}O and ^{10}B nuclides in the boron film: their high-energy edges are consistent with both nuclides starting at the surface of the target and their widths are consistent with the measured thickness of the boron target (Table 1). The form of the ^{16}O peak shows that the number of oxygen nuclides is somewhat higher at the front-side and back-side of the boron film, while the form of the ^{10}B peak exhibits a nearly uniform distribution over the target thickness, consistent with Fig. 4. Using (3), (6), and (8), and the known elastic scattering cross section, the number of ^{16}O nuclides, N_O, in the boron film was determined [18] to $N_O = (4.0\pm0.5)\times10^{17}$ atoms/cm^2. The results for all ^{10}B enriched targets are summarized in Table 1.

Since the elastic scattering cross section for the ^{10}B and ^{11}B nuclides at $E_\alpha = 7.60$ MeV and $\theta_{lab} = 165°$ is not well known [21, 22], a similar analysis for their contents in the boron film could not be carried out. However, it should be noted that the spectra obtained with the ^{10}B enriched targets showed no peak for the ^{11}B nuclides (e.g. Fig. 5a), consistent with the isotopic enrichment of the target (Sect. 4.1). The spectra also indicated that other elements are not present in the target in significant amounts, relative to B and O.

The oxygen content in the 2 boron targets of natural isotopic composition was determined [17] via the direct capture process in the $^{16}O(p,\gamma)^{17}F$ reaction [23] at

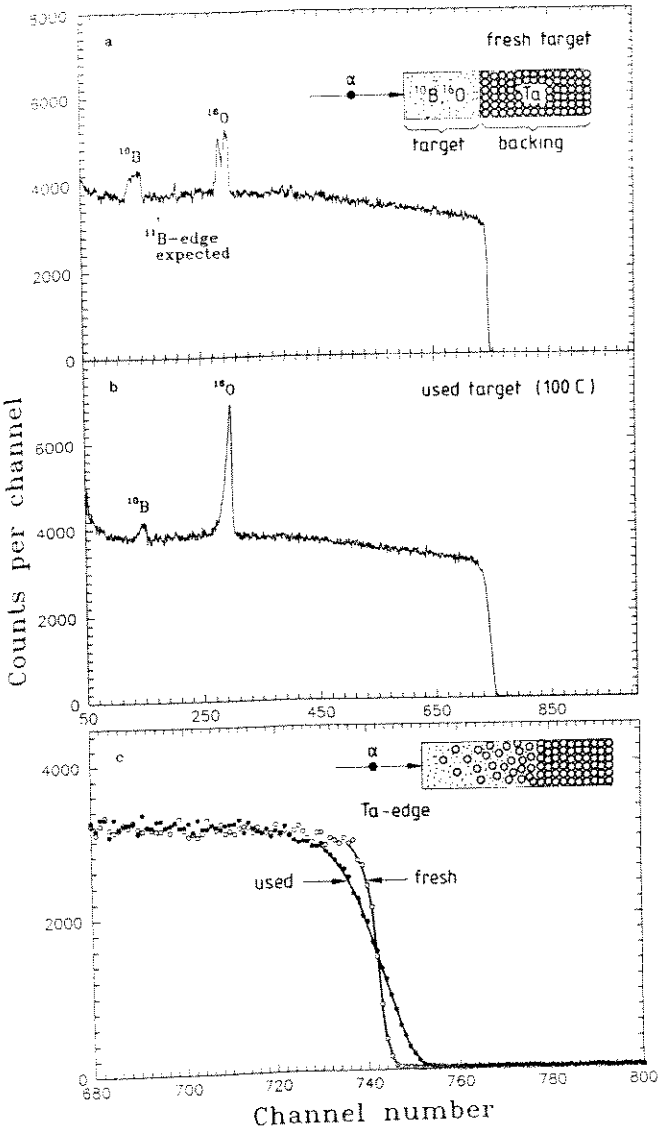

Fig. 5. a Sample spectrum of the BS-detector ($\theta_{lab} = 165°$) obtained at $E_x = 7.60$ MeV for the ^{10}B enriched target #1 ("fresh"). The spectrum is dominated by the Ta plateau, but the elastic scattering yields from the ^{10}B and ^{16}O nuclides in the boron film are also clearly visible at this bombarding energy. **b** Spectrum obtained at $E_x = 7.60$ MeV (same charge as in **a** after this same target was bombarded with low-energy protons over an accumulated charge of 100 C ("used"). **c** The change in target stoichiometry (seen in **b** as well as in Fig. 4) is also visible at the Ta edge showing a shift of the used target towards the target surface. The curves through the data points are to guide the eye only

$E_p = 1.00$ MeV using the Ge detector at $\theta_\gamma = 0°$ in close geometry (Sect. 3.3). The yield of the isotropic secondary γ-ray transition, 495→0 keV, together with the cross section, $\sigma = 1.10$ μb, and the absolute photopeak efficiency, $\kappa(E_\gamma) = 0.012$, led to the number of ^{16}O nuclides in the target. The results for both targets are summarized in Table 1.

The results for N_O together with the Δ_{eff} values led [18] to the number of boron isotopes in the target, N_B, as given in column 5 of Table 1. It was here assumed that the boron and oxygen nuclides represent the dominant constituents of the boron targets. Using the deduced N_B and N_O values and stopping power data [19], the calculated values for the target thickness were in good agreement with observation (e.g. target #1: calculation = 95 μg/cm^2; observation ≃ 100 μg/cm^2, Table 1).

4.4. Boron and carbon content in the targets

The content of ^{10}B and ^{12}C nuclides in the ^{10}B enriched targets was investigated via (d,p) and (d,α) induced reactions on these nuclides at $E_d = 0.92$ MeV using the NRA-detector at $\theta_{lab} = 135°$ (Sect. 3.3). The cross section for these reactions is well known [24–26] and exhibits a nearly constant value at this energy range and detection angle. A sample spectrum obtained for target #2 is shown in Fig. 6. The deduced numbers of boron and carbon nuclides are summarized in Table 1. The values for N_B (column 6 of Table 1) are in good agreement with the values deduced from other methods (column 5 of Table 1), and the accepted values are given in column 7 of Table 1. It turned out that the carbon nuclides (column 8 of Table 1) represent a negligible component in the target composition ($\leqq 1\%$). Again, the spectra indicated that other light elements such as Li, Be, N, and F are not present in the target in significant amounts relative to B and O.

4.5. Target deterioration at low energies

As discussed earlier (Sects. 3.2 and 4.2), thick boron targets were produced to minimize the effects of sputtering on the observed α-yields from both fusion reactions at low proton energies. To check for possible beam-induced deterioration of the targets, the α-yield at a standard energy was measured during the course of the experiments as a function of accumulated charge on a given target (approximately every 2 h of running time). The

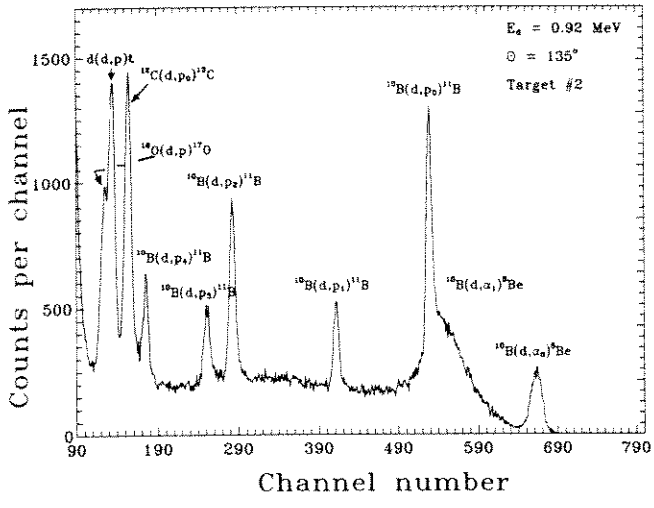

Fig. 6. Spectrum of the NRA-detector ($\theta_{lab} = 135°$) obtained at $E_d = 0.92$ MeV for the ^{10}B enriched target #2. The observed peaks originate from (d,p) and (d,α) induced reactions on the ^{10}B, ^{12}C, and ^{16}O nuclides in the target. The $d(d,p)t$ peak arises from d-implantation of the analysing beam in the target

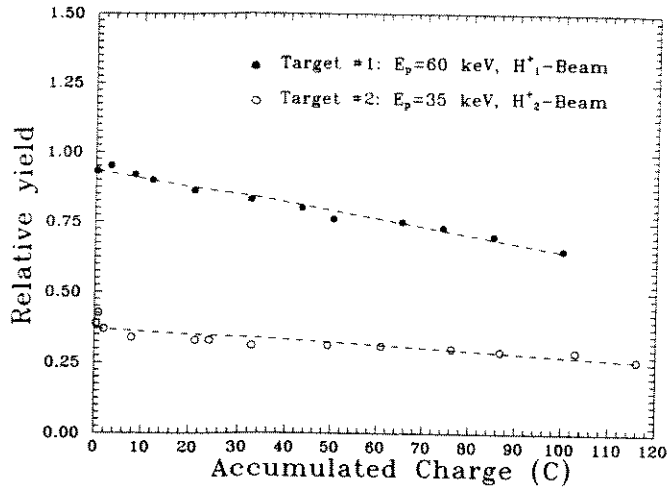

Fig. 7. Relative α-yield of the $^{10}B(p,\alpha)^{7}Be$ reaction as a function of accumulated charge on target #1 (standard energy: $E_p = 60$ keV, H_1^+ beam, 0.50 μm thick Ni foil) and target #2 (standard energy: $E_p = 35$ keV, H_2^+ beam, 0.25 μm thick Ni foil). The *dashed curves* through the data points assume a linear relationship between yield and charge

results for targets #1 and #2 are shown in Fig. 7 exhibiting a continuous yield decrease by up to about 30% for a charge of 100 C. Similar results were found [18] for the other boron targets. This target deterioration was taken into account in the analysis of the data (Sect. 4.8).

4.6. Stoichiometry of the used boron targets

In order to understand in more detail the changes in target stoichiometry, the used boron targets were investigated using BS and NRA analyses. We discuss here such measurements and results mainly for target #1 after a proton bombardment with 100 C of charge, although the conclusions apply to all used targets.

The thick target yield curve at the $E_R = 162$ keV resonance in $^{11}B(p,\gamma)C^{12}$ shows (Fig. 34) a yield decrease near the target surface of about 30% and a reduction in effective target thickness by about 39%. The 50% yield point at the front edge coincides still with the E_R value showing that no significant layers have been deposited on the surface of the target (such as carbon) during the proton bombardment. Since the low-energy yields of the fusion reactions arise mainly from the first atomic layers (the surface region) in the target (due to the nearly exponential drop in cross section), the data are consistent with the observed decrease in α-yield at the standard energy (Fig. 7).

These conclusions are further supported by the elastic scattering spectra obtained at $E_\alpha = 7.60$ MeV (Fig. 5b and c). The ^{10}B peak starts still at the target surface, but its width and height are reduced consistent with the data of Fig. 4. The ^{16}O peak also starts at the target surface, with a similar area as the fresh target, but its distribution has changed including here also partly the region of the Ta backing. The changes in the boron film are also visible at the Ta-edge (Fig. 5c) showing that the Ta atoms in the used target have moved closer to the target surface and that the interface between the boron film and Ta backing is not sharp anymore; thus, there is a growing mixture of Ta and other atoms (O and B) with increasing distance from the target surface. These observations indicate that the boron targets have changed their stoichiometry partly due to sputtering effects (reducing Δ_{eff}) and partly due to radiation enhanced diffusion (mixing of the target and backing elements).

Finally, H atoms are implanted into the target by the projectiles contributing thus additionally to possible changes in target stoichiometry. The content and distribution of the implanted H atoms were probed using the $E_R = 6.434$ MeV resonance in the $^1H(^{19}F,\alpha\gamma)^{16}O$ reaction [27] ($\Gamma_R = 44$ keV, $\omega\gamma = 22.3$ eV). The count rate of the isotropic 6.13 MeV γ-rays was observed with the Ge detector at 0° in close geometry (Sect. 3.3). Using (4) the resulting thick target yield of a narrow resonance is given by the expression [1]

$$Y_{max} = (\lambda^2/2)\,\omega\gamma\,(M_p + M_t)\,M_t^{-1}\,\varepsilon_{eff}^{-1}, \qquad (10)$$

where λ^2 is the squared DeBroglie wavelength, M_p and M_t are the masses of the projectile and target nuclides, respectively, and ε_{eff} is the effective stopping power in the lab system. The resulting thick-target yield curve for the H atoms in target #1 (after bombardment with 100 C of low-energy protons) is illustrated in Fig. 8. The data show that the H atoms start at the surface of the boron film and extend nearly homogeneously into the target with a depth of $\Delta_{eff} = 1.10 \pm 0.05$ MeV. The absolute yield of the 6.13 MeV γ-rays together with (10) led to an effective stopping power of $\varepsilon_{eff} = (1.1 \pm 0.1) \times 10^{-12}$ eV atom^{-1} cm^2. The values of Δ_{eff} and ε_{eff} led to the number of hydrogen atoms, $N_H = (1.0 \pm 0.1) \times 10^{18}$ atoms/cm^2. For the proton beam diamter of 15 mm (Sect. 3.2) this result implies that about 0.30% of the incident hydrogen

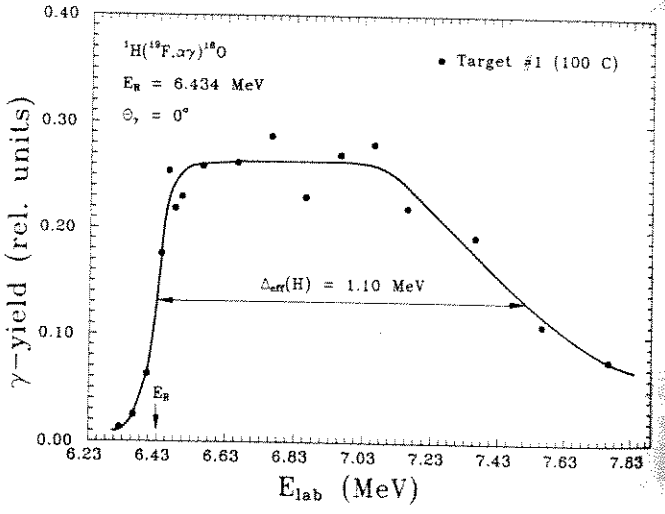

Fig. 8. Thick target yield curve of the narrow resonance at $E_R = 6.434$ MeV in $^1H(^{19}F,\alpha\gamma)^{16}O$ for the ^{10}B enriched target #1, after exposure to a low-energy hydrogen beam of 100 C accumulated charge. The hydrogen depth width is $\Delta_{eff} = 1.10$ MeV. The *solid curve* through the data points is to guide the eye only

ions are implanted into the target. Taking into account the 30% reduction in the number of boron atoms near the target surface and a similar number of oxygen atoms as in the fresh target (as discussed above), the boron film contains about 21% H atoms at the end of its irradiation (or: $N_H/N_B \simeq 0.30$). Similar results were found [18] for the other targets.

The effective stopping power relevant for the studies of the fusion reactions is thus described by the equation

$$\varepsilon_{eff} = \varepsilon_B + (N_H/N_B)_q \varepsilon_H + (N_O/N_B)_q \varepsilon_O, \quad (11)$$

where the index q indicates the accumulated charge on target. For example, at $E_p = 20$ keV one finds for target #1 values of $\varepsilon_{eff} \simeq 1.12 \times 10^{-14}$ eV atom^{-1} cm^2 for $q = 0$ and $\varepsilon_{eff} \simeq 1.25 \times 10^{-14}$ eV atom^{-1} cm^2 for $q = 100$ C. The change of about 12% in ε_{eff} is consistent with the mean yield decrease of $0.5 \times 30\% = 15\%$ observed for this target (Sect. 4.5 and Fig. 7).

4.7. *Measurement of excitation functions*

The measurement of excitation functions for both fusion reactions was carried out at the 100 and 400 kV accelerators using atomic (H^+) as well as molecular (H_2^+ or H_3^+) hydrogen beams. In the $^{10}B(p,\alpha)^7Be$ studies a H^+ beam was used at $E_p = 150$ to 35 keV, a H_2^+ beam at $E_p = 37.5$ to 30.0 keV, and a H_3^+ beam at $E_p = 28$ to 20 keV, while in the $^{11}B(p,\alpha)^8Be$ studies a H_1^+ beam was used at $E_p \geqq 35$ keV and a H_3^+ beam at lower energies. In the low-energy range data have been obtained in energy steps of $\Delta E_{lab} = 1$ keV and, at higher energies, in steps of $\Delta E_{lab} = 5$ keV. The measurement at each energy was carried out until at least a total of 1000 events was registered in the 4 Si detectors, except at the lowest energies. The running time and accumulated charge at the lowest energies was of the order of 60 h and 70 C, respectively. Background runs were carried out over a similar length of time, where the ion beam was stopped in a Faraday cup placed about 2 m in front of the target setup. During the measurements at the lowest energies, the deterioration of the target was checked approximately every 2 h by the α-particle yield at a standard energy (Sect. 4.5).

When the measurement of the excitation function for a given target was completed, the target chamber assembly was moved – without breaking the vacuum – to the 400 kV and 4 MV accelerators for investigation of beam-induced target stoichiometry (Sect. 4.6).

4.8. *Simulation of thin target yield curves*

At a given incident energy E_0 (c.m.) the number of counts observed in the 4 Si detectors ($\theta_{lab} = 130°$) was extracted [18] from the spectra in the following way. In the case of $^{11}B(p,\alpha)^8Be$ the number of counts of the α_0- and α_1-groups (e.g. Fig. 3) was obtained by summing the counts over the relevant energy regions and correcting them for the contributions of noise (exponential function) and cosmic rays, where applicable (see also [15]). In the case of the $^{10}B(p,\alpha)^7Be$ studies the number of counts in the α-peak was derived using a description (e.g. Fig. 2b) of *(i)* the noise by an exponential function, *(ii)* the cosmic or $^{11}B(p,\alpha)^8Be$ background (whatever applicable) by a constant, and *(iii)* the a-peak by Gaussian functions. The resulting count rates were finally summed and corrected [18] for dead time effects ($\leqq 2\%$) as well as for the observed yield decrease as a function of accumulated charge on target (e.g. Fig. 7). For the "infinitely" thick targets used, this count rate, $N_\infty(E_0, \theta_{lab})$, is related to the cross section via (3) and (4) with $E_{max} = E_0$ and $E_{min} = 0$. To arrive at a thin target yield, the observed count rate was corrected firstly for the number of incident projectiles (N_p), solid angle (Ω_{lab}), and the factor $(1+\delta)$:

$$N_\infty^*(E_0, \theta_{lab}) = 4\pi N_\infty(E_0, \theta_{lab})/(N_p \Omega_{lab}(1+\delta)); \quad (12)$$

Table 2. Absolute $S(E)$ factor

$^{10}B(p,\alpha)^7Be$		$^{11}B(p,\alpha)^8Be$	
E (keV)[a]	S (MeV-b)[b]	E (keV)[a]	S[c] (MeV$-b$)[b]
18.73	1860 ± 380	16.72	300 ± 67
19.64	1740 ± 380	18.54	288 ± 42
21.10	1200 ± 170	19.80	267 ± 54
22.37	960 ± 210	20.73	264 ± 48
23.28	910 ± 200	22.19	249 ± 27
24.73	509 ± 72	24.04	251 ± 25
26.52	554 ± 40	26.40	236 ± 18
28.60	589 ± 35	30.27	225 ± 13
30.85	399 ± 25	34.79	217 ± 13
33.13	422 ± 25	39.34	223 ± 13
35.39	265 ± 18	43.90	211 ± 13
37.64	338 ± 22	48.46	210 ± 13
39.91	291 ± 18	53.02	206 ± 12
43.60	220 ± 13	57.59	206 ± 12
48.06	200 ± 12	62.16	216 ± 13
51.26	138 ± 8	66.73	202 ± 12
53.53	112 ± 7	71.30	208 ± 12
55.79	161 ± 10	75.87	205 ± 12
58.07	135 ± 8	80.45	207 ± 12
60.34	149 ± 9	85.02	215 ± 13
62.61	130 ± 8	91.18	209 ± 12
64.88	102 ± 6	96.91	219 ± 13
67.15	107 ± 6	101.5	215 ± 13
69.42	101 ± 6	106.1	228 ± 14
71.69	120 ± 7	110.7	233 ± 14
75.25	70 ± 4	115.2	243 ± 14
79.79	82 ± 4	119.8	254 ± 15
84.32	69 ± 4	124.4	258 ± 15
88.86	70 ± 4	129.0	275 ± 16
93.40	70 ± 4	133.5	299 ± 18
97.94	56 ± 3		
102.5	64 ± 4		
107.0	44 ± 3		
111.6	48 ± 3		
116.1	46 ± 3		
120.6	38 ± 2		
125.2	34 ± 2		
132.3	20 ± 2		

[a] Effective energy in c.m. system (Sect. 4.8)
[b] Errors quoted arise from uncertainties in number of counts, effective energy, and target deterioration. All values have a common error of 6% due to uncertainties in N_p, Ω_{lab}, and ε_{eff}
[c] For summed α_0 and α_1 channels, where the α_0 channel contributes [18] about 1% to the total $S(E)$ factor

secondly, the resulting rates $N_{\infty}^{*}(E_0, \theta_{lab})$ obtained at adjacent energies E_{01} and E_{02} (with $\Delta = E_{01} - E_{02} \simeq 1$ to 5 keV) were subtracted and corrected for the mean solid-angle-factor $K_{\Omega}(E_0, \theta)$ in the energy interval Δ, leading thus finally to the thin target yield $Y(E_0)$ described by (5) and (7), with $E_{max} = E_{01}$ and $E_{min} = E_{02}$. The stopping power $\varepsilon_{eff}(E)$ in (7) represents in this analysis that of the fresh boron targets (Table 1). The effective energy E_{eff} within the target thickness Δ is then obtained using (7).

For illustration we take the $^{10}B(p,\alpha)^{7}Be$ studies as example. Here we have for the lowest thin target data point E_{01} (lab) = 21.00 keV and E_{02} (lab) = 20.00 keV with Δ (lab) = 1.00 keV, leading to E_{eff} (c.m.) = 18.69 keV. The effects of energy spread in the incident proton beam, energy straggling, and Doppler broadening led [18] to a total spread of $\xi_a = \pm 0.21$ keV. Since a H_3^+ molecular beam was used here, one has an additional spread of $\xi_b = \pm 0.35$ keV due to the Coulomb explosion of the molecular beam [18], leading to $\xi_{tot} \simeq (\xi_a^2 + \xi_b^2)^{1/2} = \pm 0.41$ keV. Taking this spread into account in (7), one arrives at the final effective energy $E_{eff} = E = 18.73 \pm 0.07$ keV for the lowest data point (Table 2). The error in E translates into an uncertainty in $\sigma(E)$ of 6%.

To extract the cross section $\sigma(E)$ directly from the observed thick target yields, one must assume a form of the cross section curve and calculate the yield from the integral in (5) with $a = 0$ and $b = E_0$ for each measurement. This procedure must be iterated until the $\sigma(E)$ curve, folded in the integral of (5), looks like the measured excitation function. It turned out [18] that both procedures gave consistent results.

4.9. *Absolute cross sections*

Using the procedures just described the resulting absolute cross sections $\sigma(E)$ for both fusion reactions are summarized in Table 2 in form of the $S(E)$ factor and displayed in Figs. 9 and 10. The errors quoted arise from uncertainties in number of counts, effective energy, and target deterioration. All values have a common error of 6% due to uncertainties in N_p (3%), Ω_{lab} (1%), ε_{eff} (5%).

For the $^{11}B(p,\alpha)^{8}Be$ reaction the present results are in excellent agreement with previous work [14, 15] (Fig. 9). The energy dependence of the $S(E)$ factor for $^{10}B(p,\alpha)^{7}Be$ from the present work is in contradiction to the data of [10] and [11] at overlapping energies but in fair agreement with the data from [9, 12, 13] (compare Figs. 1 and 10). Thus, only the data from the latter references have been used in Fig. 10, where the absolute scale of the data from [13] has been normalized by a factor 1.83 to that of the present work at overlapping energies.

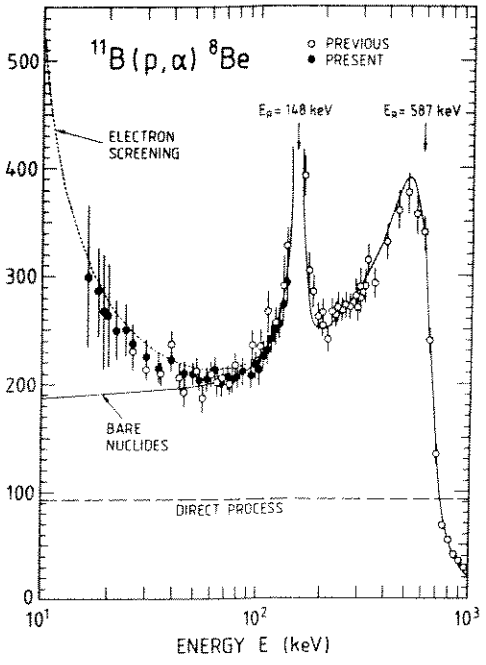

Fig. 9. Absolute $S(E)$ factor for $^{11}B(p,\alpha)^{8}Be$ as obtained from previous [15] (see also Fig. 1 for data from [14]) and present work. The *solid curve* through the data points represents a fit including 2 resonances, a nonresonant (direct) process, and interference effects. This curve simulates approximately the case of bare nuclides and has been extrapolated to lower energies. The *dashed curve* represents the enhancing effects of electron screening with $U_e = 430$ eV

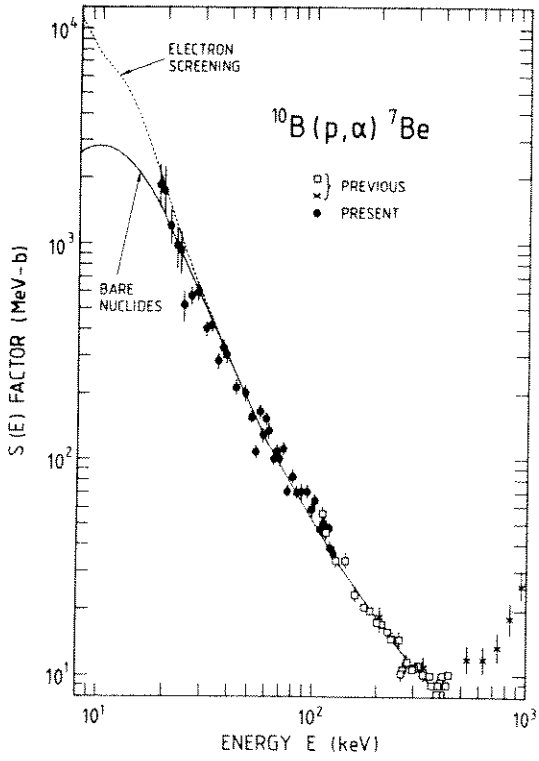

Fig. 10. Absolute $S(E)$ factor for $^{10}B(p,\alpha)^{7}Be$ as obtained from previous [12, 13] and present work (note the logarithmic scale of the ordinate). The data of [10] and [11] have been omitted (see Fig. 1). The solid curve through the data points represents a fit for a resonance at $E_R = 10$ keV ($\Gamma_R = 16$ keV) and the dashed curve includes the effects of electron screening

5. Discussion

5.1. The $^{11}B(p,\alpha)^{8}Be$ reaction

Since the effects of electron screening are expected to be negligible at energies $E \geqq 80$ keV, the data have been fitted at $E = 80$ to 1000 keV in terms of the known p-wave resonance at $E_{R1} = 148$ keV (with $\Gamma_{R1} = 5.3$ keV, $S_{R1} = 2920$ MeV b; all parameters in c.m. system, from [15]), the known s-wave resonance at $E_{R2} \simeq 620$ keV (with $\Gamma_{R2} \simeq 300$ keV, $S_{R2} \simeq 160$ MeV b; all parameters in c.m. system, from [29]), a nonresonant/direct process with $S_{NR}(E) = \text{const}$ [3] (assumed to be described predominantly by s-wave formation in the entrance channel at low energies), and an interference term between the amplitudes of the last two processes:

$$S(E) = S_{R1}(E) + S_{R2}(E) + S_{NR}(E) + 2(S_{R2}(E)\,S_{NR}(E))^{1/2}\cos\phi\,, \qquad (13)$$

where ϕ is the usual resonance phase shift [1] (here: for $R2$). The energy dependence of the resonance terms $S_{Ri}(E)$ is described [1] by the Breit-Wigner expression including the energy dependence of all partial and total widths. The free parameters in the fit were $E_{R2}, \Gamma_{R2}, S_{R2}$, and S_{NR}. The best fit (solid curve in Fig. 9) was obtained for $E_{R2} = 596 \pm 30$ keV, $\Gamma_{R2} = 383 \pm 40$ keV, $S_{R2} = 213 \pm 40$ MeV b, and $S_{NR} = 96 \pm 15$ MeV b. The calculated curve represents approximately the case of bare nuclides, $\sigma_b(E)$ or equivalently $S_b(E)$, and was extended to lower energies with $S_b(0) = 187 \pm 30$ MeV b. Finally, the low-energy data were fitted using the $S_b(E)$ curve together with the electron screening enhancement (2) leading to a screening potential energy of $U_e = 430 \pm 80$ eV.

5.2. The $^{10}B(p,\alpha)^{7}Be$ reaction

The absolute $S(E)$ values of this reaction are shown in Fig. 10 revealing a steep increase towards lower energies by more than a factor 200 compared to the data near $E \simeq 400$ keV. This steep rise cannot at all be explained by the effects of electron screening. However, there is an excited state in ^{11}C at $E_x = 8701$ keV ($J^\pi = 5/2^+$) near the proton threshold, which could represent an s-wave resonance at $E_R = 10 \pm 2$ keV with $\Gamma_R = 16 \pm 1$ keV. From the available data Youn et al. [13] had already suggested a significant contribution of this resonance to the observed yields at low energies. The resonance parameters quoted were obtained [30] from direct capture γ-ray transitions feeding this state in the $^{10}B(p,\gamma)^{11}C$ reaction. Thus, the data were described by the resonant formalisms, $S_R(E)$, including the electron screening factor, $f(E) \simeq \exp(\pi\eta U_e/E)$,

$$S(E) = S_R(E)\,f(E), \qquad (14)$$

where $S_R(E)$ represents the case of bare nuclides and $S(E)$ that of shielded nuclides. Since electron screening effects should be independent from isotopic effects [5], we have adopted $U_e = 430$ eV from the $^{11}B(p,\alpha)^{8}Be$ studies (Sect. 5.1). Further, since E_R and Γ_R are well known, the free parameter in the fit was the $S(E)$ factor at $E_R = 10$ keV, S_R. The best fit (with $S_R = (2.87 \pm 0.50) \times 10^3$ MeV b) for the case of bare nuclides is shown as a solid curve in Fig. 10, while the dotted curve includes the effects of the electron screening enhancement. The data are well described by this analysis over the whole energy range up to $E \simeq 400$ keV, while at higher energies the effects of higher-lying resonances show up in the data. Note that if data could be obtained near $E_R = 10$ keV they would not exhibit the usual shape of a Breit-Wigner curve due to the strong electron screening effects at these energies (a factor 3 and more).

5.3. Electron screening potential

The electron screening potential energy U_e (Sect. 1) was calculated using the screening distance

$$a = 0.885\, a_0\, (Z_1^{2/3} + Z_2^{2/3})^{-1/2}$$

of the Thomas-Fermi model [19], with $a_0 = 0.53$ A^0, as the atomic radius:

$$U_e(\text{in eV}) = 30.7\, Z_1 Z_2 (Z_1^{2/3} + Z_2^{2/3})^{1/2}. \qquad (15)$$

The resulting values for the systems H + He, H + Li, and H + B are compared with observed values in Table 3. Alternatively, the screening potential energy was deduced from the difference in total electron binding energy of the atoms in the entrance channel (U_p, U_t) and the compound atom (U_c):

$$U_e = U_c - U_p - U_t, \qquad (16)$$

where the atomic binding energy of an atom (within the Thomas-Fermi model) is given by

$$U_{\text{atom}}(\text{in eV}) = 15.7\, Z^{7/3}. \qquad (17)$$

The resulting values are also summarized in Table 3. Both sets of theoretical values are nearly identical and agree also well with calculated values based on improved models [7, 8]. As can be seen in the table, the experimental values are systematically higher than the expected values. This difference is not understood at present.

Table 3. Screening potential U_e

System	U_e(eV)		
	theory[a]	theory[b]	experiment
H + He	108	99	120 ± 20[c]
H + Li	180	162	420 ± 120[d]
H + B	340	304	430 ± 80[e]

[a] Using (16) and (17)
[b] Using (15)
[c] [4]
[d] [5]
[e] Present work

[3] DWBA calculations [31] are consistent with this assumption

5.4. Summary

The fusion reaction $^{11}B(p,\alpha)^{8}Be$ has been studied to energies as low as 16.7 keV, where the effects of electron screening have clearly been seen, as in other recent studies of fusion reactions involving light nuclides [4, 5]. The effect is however larger – in all cases studied so far – than can be understood at present from available models. The $S_b(E)$ factor for bare nuclides is understood over a large energy region in terms of resonances and a nonresonant process, including interference effects. The extrapolated value at zero energy is $S_b(0) = 187$ MeV b, in good agreement with previous work [14, 15].

The fusion reaction $^{10}B(p,\alpha)^{7}Be$ has been investigated as low as 18.7 keV and its $S(E)$ factor shows a steep increase with decreasing energy. It has been shown that the expected resonance at $E_R = 10$ keV is responsible for this steep rise and that it dominates the $S(E)$ factor up to an energy of about 400 keV. The effects of electron screening improve the fit to the data at very low energies and it must be taken into account to arrive at the correct relevant resonance cross section for bare nuclides.

Peterson et al. [16] have considered various fusion reactions involving light nuclides as alternative clean fuels in future fusion reactors. Among the boron isotopes the $^{11}B(p,\alpha)^{8}Be$ reaction was discussed, while the $^{10}B(p,\alpha)^{7}Be$ reaction was only discussed in terms of its (mild) radioactivity, due to the residual ^{7}Be nuclides ($T_{1/2} = 53$ d, $E_\gamma = 478$ keV). However, the present work has shown that the $S(E)$ factor of this reaction – for bare nuclides – is about a factor 15 higher than that of $^{11}B(p,\alpha)^{8}Be$ at $E = 10$ keV, improving significantly its perspective as alternative fuel in terrestrial fusion reactors. Since the $^{10}B(p,\alpha)^{7}Be$ reaction can also proceed via the first excited state of ^{7}Be at 429 keV, with $Q = 717$ keV, this reaction channel could further enhance the total cross section. An experimental investigation of this reaction channel (via γ-ray spectroscopy of the 429 keV secondary transition) is in preparation. Note that the 10 keV resonance corresponds to a plasma temperature of only 4.9×10^6 K.

The authors would like to thank H.W. Becker, K. Langanke, and H.P. Trautvetter for many discussions and H. Baumeister and B. Hippert for the production of the boron targets. We are also grateful to M. Bahr, M. Berheide, U. Greife, M. Junker, J. Meijer, G. Quathamer, G. Roters, T. Schange, S. Schmidt, and D. Zahnow for help during the course of the experiments. We also thank M. Wielunski for assistance in the analyses of the boron targets and M. Buschmann for help in the data analysis.

References

1. Rolfs, C., Rodney, W.S.: Cauldrons in the cosmos. Chicago: University of Chicago Press 1988
2. Assenbaum, H.J., Langanke, K., Rolfs, C.: Z. Phys. A**327**, 461 (1987)
3. Langanke, K., Rolfs, C.: Mod. Phys. Lett. A**4**, 2101 (1989)
4. Engstler, S., Krauss, A., Neldner, K., Rolfs, C., Schröder, U., Langanke, K.: Phys. Lett. B**202**, 179 (1988)
5. Engstler, S., Raimann, G., Angulo, C., Greife, U., Rolfs, C., Schröder, U., Somorjai, E., Kirch, B., Langanke, K.: Z. Phys. A**342**, 471 (1992)
6. Blüge, G., Langanke, K., Reusch, H.G., Rolfs, C.: Z. Phys. A**333**, 219 (1989)
7. Bracci, L., Fiorentini, G., Melezhik, V.S., Mezzorani, G., Quarati, P.: Nucl. Phys. A**513**, 316 (1990)
8. Bencze, G.: Nucl. Phys. A**492**, 459 (1989)
9. Burcham, W.E., Freeman, J.M.: Philos. Mag. **40**, 807 (1950); ibid **41**, 337 (1950)
10. Bach, G.C., Livesey, D.J.: Philos. Mag. **46**, 824 (1955)
11. Szabo, J., Csikai, J., Varnagy, M.: Nucl. Phys. A**195**, 527 (1972)
12. Roughton, N.A., Fritts, M.J., Peterson, R.J., Zaidins, C.S., Hansen, C.J.: At. Data Nucl. Data Tables **23**, 177 (1979)
13. Youn, M., Chung, H.T., Kim, J.C., Bhang, H.C., Chung, K.H.: Nucl. Phys. A**533**, 321 (1991)
14. Davidson, J.M., Berg, H.L., Lowry, M.M., Dwarakanath, M.R., Sierk, A.J., Batay-Csorba, P.: Nucl. Phys. A**315**, 253 (1979)
15. Becker, H.W., Rolfs, C., Trautvetter, H.P.: Z. Phys. A**327**, 341 (1987)
16. Peterson, R.J., Zaidins, C.S., Fritts, M.J., Roughton, N.A., Hansen, C.J.: Ann. Nucl. Energy **2**, 503 (1975)
17. Angulo, C.: Diplomarbeit, Universidad de Sevilla (1991)
18. Angulo, C.: Thesis, Universidad de Sevilla (1992)
19. Ziegler, J.F., Biersack, J.P., Littmark, U.: The stopping and range of ions in solids. New York: Pergamon Press 1985
20. John, J., Aldridge, J.P., Davis, R.H.: Phys. Rev. **181**, 1455 (1969)
21. David, P., Debrus, J., Mommsen, H., Riccato, A.: Nucl. Phys. A**182**, 234 (1972)
22. Ott, W.R., Weller, H.R.: Nucl. Phys. A**198**, 505 (1972)
23. Rolfs, C.: Nucl. Phys. A**217**, 29 (1973)
24. Vis, R.D.: Nucl. Instrum. Methods B**66**, 139 (1992)
25. Marion, J.B., Weber, G.: Phys. Rev. **103**, 1408 (1956)
26. Purser, K.H., Wildenthal, B.H.: Nucl. Phys. **44**, 22 (1963)
27. Becker, H.W., Kieser, W.E., Rolfs, C., Trautvetter, H.P., Wiescher, M.: Z. Phys. A**305**, 319 (1982)
28. Knape, F., Bucka, H., Heide, P.: Technische Universität Berlin (Private communication, 1992)
29. Ajzenberg-Selove, F.: Nucl. Phys. A**433**, 1 (1985)
30. Wiescher, M., Boyd, R.N., Blatt, S.L., Rybarcyk, L.J., Spizuoco, J.A., Azuma, R.E., Clifford, E.T.H., King, J.D., Görres, J., Rolfs, C., Vlieks, A.: Phys. Rev. C**28**, 1431 (1983)
31. Raimann, G.: (to be published)